HHS Public Access

Author manuscript

Nat Chem Biol. Author manuscript; available in PMC 2017 February 22.

Published in final edited form as:

Nat Chem Biol. 2016 October ; 12(10): 860–866. doi:10.1038/nchembio.2159.

Oxidation increases the strength of the methionine-aromatic interaction

Andrew K. Lewis[1], **Katie Dunleavy**[2], **Tiffany L. Senkow**[1], **Cheng Her**[4], **Benjamin T. Horn**[2], **Mark A. Jersett**[2], **Ryan Mahling**[2], **Megan R. McCarthy**[4], **Gabriella T. Perell**[3], **Christopher C. Valley**[1], **Christine B. Karim**[4], **Jiali Gao**[3], **William C. K. Pomerantz**[3], **David D. Thomas**[4], **Alessandro Cembran**[2,*], **Anne Hinderliter**[2,*], and **Jonathan N. Sachs**[1,*]

[1]Department of Biomedical Engineering, University of Minnesota – Twin Cities, Minneapolis, MN 55455

[2]Department of Chemistry and Biochemistry, University of Minnesota – Duluth, Duluth, MN 55812

[3]Department of Chemistry, University of Minnesota – Twin Cities, Minneapolis, MN 55455

[4]Department of Biochemistry, Molecular Biology, and Biophysics, University of Minnesota – Twin Cities, Minneapolis, MN 55455

Abstract

Oxidation of methionine disrupts the structure and function of a range of proteins, but little is understood about the chemistry that underlies these perturbations. Using quantum mechanical calculations, we show that oxidation increases the strength of the methionine-aromatic interaction motif—a driving force for protein folding and protein-protein interaction—by 0.5 – 1.4 kcal/mol. We find that non-hydrogen bonded interactions between dimethyl sulfoxide (a methionine analog) and aromatic groups are enriched in both the Protein Data Bank and Cambridge Structural Database. Thermal denaturation and NMR experiments on model peptides demonstrate that oxidation of methionine stabilizes the interaction by 0.5–0.6 kcal/mol. We confirm the biological relevance of these findings through a combination of cell biology, electron paramagnetic resonance spectroscopy and molecular dynamics simulations on 1) calmodulin structure and dynamics and 2) lymphotoxin-α/TNFR1 binding. Thus, the methionine-aromatic motif is a determinant of protein structural and functional sensitivity to oxidative stress.

*Co-corresponding authors: jnsachs@umn.edu.

Author contributions

Project conception and production directed by J.N.S. PDB search, molecular dynamics simulations, experimental and computational LTα work, and computational CaM work were performed by A.K.L., T.L.S., C.C.V. and J.N.S. CSD search and NMR were performed by G.T.P. and W.C.K.P. Quantum calculations were performed by M.A.J., A.C, and J.G.. CD was performed by R.M., B.T.H., K.D. and A.H. Peptides were synthesized by C.B.K. CaM work was carried out by M.R.M, C.H., and D.D.T.

Competing financial interests

The authors declare no competing financial interests

Introduction

The methionine-aromatic motif is a promiscuous, highly stabilizing, and prevalent non-covalent interaction that forms between methionine thioether sulfurs and the aromatic rings of nearby (~5 Å) tyrosine, tryptophan, and phenylalanine residues[1–6]. Methionine-aromatic interactions have been detected in several bioinformatics studies[5,6], including our exhaustive analysis of the Protein Databank (PDB)[1]. Sulfur-aromatic (S/Ar) interactions between the C-S-C divalent sulfur motif and aromatic groups have been similarly found in the Cambridge Crystal Structural Database (CSD)[2]. The motif is substantially stronger than a purely hydrophobic contact, suggesting that it plays a unique role in stabilizing protein structure and ligand-receptor binding[1]. A thermal unfolding experiment using a synthetic helical peptide measured the Met-Phe interaction at −0.65 ± 0.15 kcal/mol[7], and quantum calculations have revealed an interaction energy of 1–3 kcal/mol at a range of 4–6 Å between dimethyl sulfide (DMS) and benzene[4]. Our own quantum calculations expanded the analysis to include DMS interactions with phenol and indole (tyrosine and tryptophan analogs, respectively) and determined that dispersion interactions are the major contributor to stability[1].

In addition to forming highly stabilizing interactions with aromatic residues, methionine is uniquely important because its thioether can undergo modification with the addition of one or two sulfonyl oxygens to become methionine sulfoxide (Met^{Ox}) or sulfone, respectively, in oxidizing environments[8]. Elevated levels of methionine sulfoxide have been detected in diseased tissues, but methionine sulfone is rare[9]. Methionine sulfoxidation is known to regulate the activity of certain proteins, while in other cases, methionine-rich domains protect critical amino acids from oxidation by removing free radicals and regulating the local redox environment[10].

Despite this functional significance, the specific molecular mechanism through which proteins sense and respond to oxidative modification of methionine residues has not been fully characterized. It has been posited that polarization of the methionine thioether by oxidation could weaken the methionine-aromatic interaction by ablating the hydrophobic contribution[11], but this has never been tested experimentally. In the present study we will show the opposite to be true – that oxidation of methionine strengthens its interaction with aromatic residues, and that this has the potential to disrupt native conformation and alter protein function. Importantly, we show that the interaction is strengthened even in the absence of a hydrogen bond between the sulfoxide oxygen (acceptor) and donor hydrogens (on Tyr or Trp). Through quantum mechanical calculations, we show that the interaction between the dipole moment of dimethyl sulfoxide (DMSO) and the aromatic ring quadrupole moment is the main contribution to the increased stability of the motif.

We start by analyzing both the PDB and the CSD to identify and characterize interactions between DMSO (a small molecule analog to Met^{Ox}) and aromatic groups in the crystal structures of proteins and small molecules. We then performed quantum mechanical calculations on model compounds to determine the strength of the sulfoxide-aromatic interaction, and assessed the potential contribution of hydrogen bonding on the motif in a variety of solvent environments. We then isolated and determined the strength of the specific

interaction between unoxidized and oxidized methionine and the sidechain of phenylalanine by extending a previously described helix unfolding experiment and performing a double mutant cycle analysis[7]. We investigated the effects of site-specific methionine oxidation on the methionine-aromatic interaction in two biologically important proteins. First, using a combination of electron paramagnetic resonance (EPR) spectroscopy and replica-exchange molecular dynamics (REMD) simulations, we probed the effects of oxidation on the structure of calmodulin (CaM). Second, we investigated lymphotoxin-α (LTα) binding to tumor necrosis factor receptor 1 (TNFR1), which we previously showed is stabilized by a methionine-aromatic interaction between M120 of LTα and W107 of TNFR1[1].

Results

DMSO-aromatic interactions in crystal structure databases

To find examples of sulfoxide-aromatic interactions, we searched the PDB and CSD for occurrences of DMSO molecules near aromatic rings (Fig. 1). The PDB is a repository containing crystal structures of proteins and the CSD is the analogous repository for organic and metal-organic small molecules. DMSO solubilizes tryptophan more readily than leucine, alanine, and glycine[12], so we expected to find that it specifically interacts with aromatic sidechains. Our PDB search yielded 205 unique structures containing a total of 872 DMSO molecules. Fig. 1a shows a representative DMSO-tyrosine interaction. When compared to all amino acids, or just the aliphatic amino acids, aromatic residues are enriched 4–7 Å from DMSO sulfurs, with a maximum at 5Å, resembling the radial density function for methionine-aromatic interactions from our previous study[1] (Fig. 1b). 451 (51.7%) DMSO molecules were found within 7 Å of the nearest aromatic residue. Only 32 of these (7.1%) are in position to accept a hydrogen bond from either tryptophan or tyrosine. Thus, hydrogen bonding does not drive DMSO-aromatic bonding in the PDB. Our CSD search similarly found an ~50% enrichment of DMSO-aromatic contacts (representative example, Fig. 1c) compared to C-CH_2-C-aromatic pairs (Fig. 1d), which were used previously as a non-interacting control to show the enrichment of the Met-aromatic motif[2]. Again, few DMSO/phenol or DMSO/indole pairs are in position to form a hydrogen bond (<14%).

We then parsed the frequency of methionine-aromatic interactions in the PDB <7 Å between DMSO and the center of phenylalanine, tyrosine, and tryptophan individually. Figure 1e shows that the interaction is more prevalent with Tyr and Trp than with Phe when normalized by the relative abundance of each of these amino acids in the analyzed structures. This trend is not explained by relative solvent accessibility, as Trp and Phe have similar solvent accessibilities, while that of Tyr is somewhat higher[13]. We calculated a 1.3 and 1.4 fold preference for tyrosine and tryptophan over phenylalanine, respectively, translating to a ~0.3 kcal/mol increase in Met^{Ox}-Tyr and Met^{Ox}-Trp stability compared to Met^{Ox}-Phe. Therefore, these database results suggest that, although hydrogen bonding is not common in the interaction motif, DMSO interacts more favorably with tyrosine and tryptophan than with phenylalanine. This has similarly been observed in cation-π interactions in proteins, where the more electron-rich Pi systems of tryptophan and tyrosine relative to phenylalanine make them more attractive to positively charged ligands[14].

Oxidation strengthens interaction in quantum calculations

The interaction energies between the reduced (DMS) and oxidized (DMSO) models of methionine with the model aromatic compounds benzene, phenol, and indole are reported in Table 1 and Supplementary Results, Supplementary Table 1. The data show that upon oxidation of DMS to DMSO the complex with benzene is 0.9 kcal/mol more stable. To understand the origin of this stabilization we first tested the possible contribution of dispersion interactions. The results (see Supplementary Table 2) show that the dispersion energy contribution for DMS/benzene is −8.4 kcal/mol, and for DMSO/benzene it is −8.2 kcal/mol. This change in contribution is small (0.2 kcal/mol) and is more stabilizing for the DMS/benzene interaction than for the DMSO/benzene. Therefore dispersion interactions are not the source of the stronger interaction energy in the oxidized complex. Rather, the stronger interaction can be explained in terms of the interaction between the dipole moment of DMSO and the aromatic ring quadrupole moment. The calculated dipole moment for DMS is 1.8 Debye, while in DMSO the enhanced polarization due to the presence of oxygen results in a dipole moment of 5.0 Debye roughly aligned along the S=O bond. Furthermore, both DMS and DMSO maximize dispersion interactions with the benzene ring by aligning the Me-S-Me moiety over the ring plane; as a result, in the DMS/benzene complex the orientation of the small dipole of DMS is orthogonal to the benzene quadrupole moment, while in DMSO/benzene the angle between the S=O bond and the ring is approximately 120°, which is well poised for a favorable dipole/quadrupole interaction. The Natural Bond Orbital (NBO) charge analysis for the complex and isolated species (Supplementary Table 3 and Supplementary Fig. 1) supports this explanation, showing a large positive charge (+1.19 e) on the sulfur that can interact with the ð electron cloud, balanced by a negative charge (−0.96 e) on the oxygen pointing away from the benzene ring (Supplementary Figure 2).

Table 1 shows that for phenol and indole the change in interaction energy upon DMS oxidation (−5.7 and −5.3 kcal/mol, respectively) is of larger magnitude than for benzene. Such a large change cannot be explained in terms of enhanced dipole/quadrupole interactions, and is a result of hydrogen bonding between the DMSO oxygen and the hydrogen of the phenol hydroxyl group or the indole amine (Supplementary Figure 2). To determine the relevance of hydrogen bonding in sulfoxide-aromatic interactions in a range of environments, we ran molecular dynamics simulations of DMSO and phenol or indole in hexane, ethyl acetate (EtOAc), or TIP3P water using the adaptive biasing force (ABF) module in NAMD. We found (Supplementary Figure 3) that DMSO hydrogen bonded with phenol and indole in hexane. Thus, in this nonpolar environment we expect the contribution of the hydrogen bond to outweigh the increased interaction energy of the S/Ar motif. Importantly, in EtOAc (a polar non-protic solvent with dielectric constant of 6, representative of the protein interior), hydrogen bonding occurred less frequently. Therefore, the S/Ar motif plays a role in the stabilization of the complex in this environment. Finally, in water hydrogen bonding between DMSO and the aromatic group was essentially absent, rather the sulfonyl and aromatic hydrogens were solvated by water. This environment mimics interfacial residues on the protein, which are often involved in protein-protein interactions[15].

To disentangle the energy contribution due to hydrogen bonding from that of sulfur-aromatic interaction, we performed quantum mechanical calculations on configurational ensembles from our simulations in EtOAc. Benzene and DMS systems were also run to compare to the full optimization calculations. EtOAc's intermediate dielectric constant and its ability to accept hydrogen bonds allows DMSO-phenol/indole complexes to sample hydrogen-bonded and non-hydrogen-bonded conformations with similar probability. We analyzed non-hydrogen bonded and hydrogen bonded ensembles as mimics of the interactions on the protein surface and in its hydrophobic core, respectively. The results (Table 1, Figure 1f) agree with the data from the full optimization, and together indicate that (a) in the absence of hydrogen bond, oxidation of DMS to DMSO strengthens the sulfur-aromatic interaction by 0.5 – 1.5 kcal/mol, and (b) in hydrogen bonded structures (rare in proteins) the complex is stabilized by up to 8 kcal/mol.

Evaluation of Oxidation in a Model Peptide Scaffold

To experimentally assess the database findings and quantum results, we utilized thermal denaturation (monitored with CD) and NMR to investigate a previously reported 15-residue peptide scaffold[7], designed such that the strength of the interaction between *i, i+4* amino acids determines the thermal stability of the peptide secondary structure. In that study, the Met-Phe pair was found to interact (ΔG_{int}) with 0.65 kcal/mol. We first confirmed a direct interaction between oxidized Met and Phe (Supplementary Table 4) using NMR. As shown in Figure 2a, we observed the strongest NOEs to the aryl hydrogens meta to the sidechain methylene (3,5 position) (Supplementary Figure 4). NOEs to the hydrogen at the 4 and 2,6 positions are present at lower levels and overlap.

To further probe the details of the sulfoxide-aromatic (S^{Ox}/Ar) interaction in the helical state, we compared the chemical shift of the ε-S-methyl groups on the sulfoxide-containing peptide when it is in an *i* +4 relationship with phenylalanine (F-MetO) versus alanine (A-MetO) in methanol. Oxidized peptides were purified as a 1:1 mixture of diastereomers due to the new stereocenter from the sulfoxide. As such, two singlets corresponding to the methyl group of each diastereomer were observed (Figure 2b). DMSO methyl resonances in methanol are reported at 2.65 ppm[16]. Similarly, in our measurements for A-MetO they are found at 2.65 and 2.64 ppm. However, for F-MetO, we observe both ε-S-methyl resonances shifted upfield at 2.57 and 2.47 ppm. Interestingly, the chemical shift of the DMSO methyl resonances in benzene have also been shown to be significantly upfield at 1.68 ppm[16]. Due to ring current shielding effects from aromatic rings, we interpret these results to be consistent with the ε-S-methyl groups of oxomethionine approaching from above the aromatic ring of phenylalanine (Figures 1a,c). Both the NOE experiments and chemical shift information indicate an interaction between the sulfoxide group over top of the aromatic ring.

We then used CD to measure the change in the strength of the S/Ar interaction upon methionine oxidation. Our experiments reproduced the original S/Ar result for Met-Phe (ΔG_{int}=0.62 kcal/mol). The interaction strength was doubled (strengthened by 0.62 kcal/mol) upon methionine oxidation. Associated with this change in free energy, we find that oxidation increases the enthalpy of the S/Ar interaction by 1.1 kcal/mol (Supplementary

Figure 5), consistent with the quantum result. We note that while CD spectra were used in the original S/Ar study to extract energetics of side-chain interactions, it is not possible to draw a direct correlation between peptide helicity and free energy[7,17]. Rather, fitting of the CD spectra is necessary to extract energetics. Two aspects of our approach differed from the original study. First, we performed a double mutant cycle to isolate the methionine-aromatic interaction from possible interference due to neighboring residues (Supplementary Table 4, Supplementary Figure 6). This approach solidifies our reported interaction free energies, and is especially important in the case of oxidized methionine because of the increased likelihood of hydrogen bonds and electrostatic interactions with the other residues in the peptide.

Second, we followed Greenfield[18] by fitting the temperature-dependence of each CD spectrum (Supplementary Figure 7) to the Gibbs-Helmholtz equation (GHE, Supplementary Figure 5). We justify applying a two-state approximation and hence using the GHE by: 1) observation of complete reversibility (overlap) in the heating and cooling curves (Supplementary Figure 8); and 2) the presence of a molar ellipticity isodichroic point in all constructs[19] (Supplementary Figure 7, inset). Additionally, principal component analysis[20] of the CD spectra yielded only two components that dominated the CD spectra (Supplementary Figure 9 and Supplementary Table 5), again consistent with the two-state assumption. Together with the addition of the double mutant cycle, the fact that we obtained nearly identical values for the Met-Phe energy as in the original study[7] (compare 0.62±0.09 to 0.65 kcal/mol) reinforces the robustness of our approach. Thus, our peptide study lends experimental support to the conclusions drawn from the quantum calculations: oxidation increases the strength of the methionine-aromatic interaction.

Oxidation rearranges Met-aromatic contacts in Calmodulin

In order to test the impact of the increased strength of the S^{Ox}/Ar motif in proteins, we first investigated the effects of methionine oxidation in an already well-characterized protein, CaM. The C-terminal helix of CaM has a high methionine content and is sensitive to oxidative stress *in vivo*, which alters the protein's structure and function[21–26]. In the crystal structures of CaM, both in its calcium-bound (halo, 3CLN)[27] and unbound (apo, 1CFD)[28] forms, a C-terminal methionine forms an S/Ar interaction with F141 (M144 in apo (Fig. 3a) and M145 in halo). It has been speculated previously that oxidation at M144 and M145 might destabilize the protein by altering an important, nearby hydrogen bond between Y138 and E82 that connects the short C-terminal helix to the central linker[24,29]. No specific molecular mechanism for this effect has been proposed or tested.

Based on our results above, one possibility is that oxidation of M144 and/or M145 increases the likelihood of an S^{Ox}/Ar interaction with Y138, which would be manifest in a spatial rearrangement within the C-terminal domain that should be observable by EPR. As M144/145 and Y138 are on opposite ends of a short helix, such an interaction would require helical unwinding, an effect that has been observed using NMR[30]. Replica exchange molecular dynamics simulations (REMD) of the isolated, Ca^{2+}-free (apo) C-terminal peptide fragment (residues 136–146) of CaM were used to guide the design and interpretation of experimental EPR measurements on full-length protein. We simulated both the unoxidized

and doubly oxidized (at M144 and M145) forms. Because of the expectation of helical unwinding, a computational investigation of full-length CaM is hampered by limitations in sampling efficiency. Thus, while the peptide fragment is an abstraction of the real system, it is nevertheless a useful tool because it accelerates the sampling of relevant conformational space. Furthermore, the simulations were useful in 1) establishing V136 and T146 as appropriate sites for spin-labels to test the impact of oxidation on the full-length protein; and 2) providing molecular scale details unavailable from EPR that correlate distance changes to the potential presence of an S^{Ox}/Ar motif.

In the simulation of the unoxidized peptide, an S/Ar interaction formed between Y138/M144 or Y138/M145 only 3.3% of the time. On the other hand, an S^{Ox}/Ar interaction formed 22.7% of the time when both M144 and M145 were oxidized (Fig 3b, Supplementary Fig. 10). In only 1.2% of these interactions did a hydrogen-bond form (Supplementary Fig. 11). As can be seen in Figure 3b, the S^{Ox}/Ar interaction with Y138 leads to a spatial rearrangement that brings together residues V136 and T146. The distribution of the distance between the Cα atoms of those two residues is shown in Figure 3c. Likewise, the frequency of the native interaction between M144 and F141 is also increased upon oxidation (49% *vs.* 12% of frames, Supplementary Fig. 10). Thus, oxidation increased the total percentage of simulated frames in which an S/Ar interaction occurs by 3.7-fold (72% *vs.* 15%). Based on Boltzmann's law, this change reflects a roughly 1.6 kcal/mol increase in the free energy of the interaction upon oxidation. This value compares well to the results of our peptide experiment (0.62 kcal/mol) and supports the underlying conclusion of increased interaction strength upon oxidation of the S/Ar motif, even absent hydrogen bonds. It is important to note that the simulations of the short, unoxidized peptide fragment sample unfolded conformational states that are not represented by the crystal structure (where residues 138–146 are helical) and may not be accessible in a simulation of the full-length protein. Nonetheless, the emergence of a second population of states containing the S^{Ox}/Ar motif (with Y138)—only in the oxidized simulation—motivated experiments to explore whether this subpopulation exists in the full-length protein when oxidized.

To test the effects of oxidation of CaM's C-terminal helix in the full-length protein, we used dipolar EPR spectroscopy to detect intramolecular structural perturbations at submicromolar [Ca2+]. The intramolecular distance distributions detected by EPR are shown in Fig. 3d. As shown in Supplementary Figure 12, the EPR spectrum of the unoxidized protein was best fit to a single broad Gaussian distance distribution, centered at 13.7 Å. After methionine oxidation, the data were best fit to a two-population model in which one population is centered at a similar distance to that observed in the absence of oxidation (14.0 Å), and there is a new population at shorter distance (8.9 Å). These experimental EPR results confirm key predictions from MD simulations (Fig. 3c): the long-distance population becomes narrower, and a new well-ordered short distance emerges. It is not surprising that the EPR distance distributions do not match precisely those predicted by MD simulation, since the MD simulations report distances between Cα atoms, while EPR distances are between nitroxide groups at the ends of flexible side chains. EPR spectra do not directly detect Cα-Cα distances, but changes in such distances have been shown to correlate well with EPR data[31]. The convergence of the simulated and experimental results strongly suggests that upon oxidation of CaM a new S^{Ox}/Ar interaction forms between either M144/Y138 or M145/

Y138. Work still remains to definitively show that this minor component in the overall accessible conformational space (Figs 3c and 3d) is responsible for disruption of the Y138/E82 hydrogen bond and alters the protein's function.

Oxidation of LTα prevents ligand/receptor binding

We investigated the effects of oxidation on the bioactivity and binding of LTá and TNF in live cells. We have previously shown that the interaction between LTá and TNFR1 is stabilized by a methionine-aromatic interaction via M120 of LTá and W107 of TNFR1. Mutation of M120 to alanine interrupts ligand binding, resulting in a >10 fold loss in ligand function[1]. Thus, we hypothesized that the increased strength of the S/Ar interaction upon oxidation should stabilize binding via the M120/W107 interaction. Tumor necrosis factor (TNF) is structurally homologous to LTá and similarly activates TNFR1, but notably lacks methionine residues. Therefore, we expected its action to be unaffected by oxidative stress. Western blot analysis (Fig. 4a) showed that untreated LTá and TNF efficiently induced downstream signaling, as has been definitively established. Surprisingly, LTá pretreated with H_2O_2 failed to induce IêBá degradation.

In order to isolate the impact of oxidation of M120 on LTá function and binding, we mutated the methionines at residues 20 and 133 to remove their susceptibility to oxidization (see Methods for details). This mutant ligand—denoted here as M120 or $M^{Ox}120$ when oxidized—triggered IêBá degradation in the unoxidized form to the same extent as wild-type (indicating that two other mutated methionine residues, M20 and M133, are not important for activity). Site-specific oxidation ($M^{Ox}120$) rendered LTá inactive (Fig. 4a). Co-immunoprecipitation experiments explain this loss in function as a result of lost binding of the $M^{Ox}120$ ligand to TNFR1 (Fig. 4b). Thus, we conclude that oxidation of LTá inhibits its activity by disrupting the critical M120-W107 methionine-aromatic interaction, thereby preventing binding to TNFR1.

To explore the molecular basis for this loss in binding, and to explain this apparent contradiction (decreased binding despite increased S/Ar interaction strength), we used molecular dynamics simulations and quantum calculations. Analysis of the ligand/receptor crystal structure (1TNR) revealed aromatic residues in the ligand (Y96 and Y122) that are near to and on the same chain as M120 (Fig. 5a). Given their spatial proximity, it is likely that M120 forms S/Ar contacts with either or both of these tyrosines. MD simulations of the unbound ligand showed this to be the case in approximately 70% of the simulated frames (the M120-Y122 interaction was approximately twice as frequent as the M120-Y96 interaction). Oxidation of M120 increased the interaction strength of M120 with Y96—again using the Boltzmann equation we calculate an increased affinity of 0.35 kcal/mol. This value is lower than that described above for CaM, but once again is consistent with our general conclusion that oxidation strengthens S/Ar interactions. Interestingly, there was no oxidation-induced change in the frequency of M120/Y122 contacts. These data raise the possibility that Y122 and Y96 interact differently with M120 under oxidative conditions. We confirmed that hydrogen bonding was not a major factor in the interaction (Supplementary Fig. 13). We again used the simulations to generate an ensemble of configurations for quantum energy calculations. A snapshot from the oxidized ensemble is shown in Figure 5b.

As was the case with our calculations on the non-hydrogen-bonded ensemble of DMS/DMSO-phenol configurations, oxidation increased the strength of the S/Ar interaction by 1–2 kcal/mol (Fig 5c).

We hypothesized that the strengthened M^{Ox}120/Y96 interaction could lock the ligand in a configuration that prevents M^{Ox}120/W107 interaction, thereby interrupting binding. To test this, we first needed to show that the addition of a sulfonyl oxygen to M120 in the crystal structure binding configuration does not itself destabilize the binding pocket by steric overlap or electrostatic repulsion. We first simulated the unoxidized crystal structure of the ligand-receptor complex. Figure 5d highlights the stability of the M120/W107 interaction, and shows the infrequent instances of M120 interaction with either Y122 or Y96. We then started a simulation of the ligand-receptor complex in a configuration in which the M^{Ox}120/Y122 pair was pre-formed (using a configuration generated from the unbound ligand simulation). Y96 was allowed to remain in its receptor backbone binding position. The binding cavity organization reverted to that of the crystal structure configuration after 50ns (Fig. 5d) and was stable throughout the remainder of the simulation (Supplementary Fig 14). Therefore, we conclude that loss of ligand-receptor binding is not caused by intrinsic steric clashes with M^{Ox}120 that disrupt the binding pocket. We also conclude that M^{Ox}120/Y122 interactions do not prevent M^{Ox}120/W107 interactions and ligand binding.

We then started a second oxidized ligand-receptor simulation, this time with a pre-formed M^{Ox}120-Y96 pair. We observed two distinct effects of oxidation, both of which are consistent with loss of receptor binding. In two of the three chains (of the symmetric ligand trimer), M^{Ox}120 remained stably bound to Y96, preventing it from forming the critical S/Ar motif with W107 (Fig. 5d) and also preventing Y96 from binding the receptor backbone. In these cases, the M^{Ox}120/Y96 pairing (Fig. 5e), along with the surrounding binding pocket, remained stable throughout the simulation. In the remaining chain, Y96 released from M^{Ox}120, and in this process disrupted the binding pocket while ejecting the receptor. Collectively, the results suggest that increased stability of the M^{Ox}120/Y96 pair prevents the critical M120/W107 interaction and destabilizes the bound state.

Discussion

Oxidative stress plays a prominent role in a number of normal and pathological biological functions. However, the precise chemical and physical mechanism through which oxidative modification of proteins influences their structures and functions is largely unknown. We have shown that oxidation of methionine strengthens the methionine-aromatic interaction motif, independent of hydrogen bonding, by at least 0.5 kcal/mol and up to 1.5 kcal/mol. In the vast majority of instances in the PDB and CSD as well as the two proteins studied here in detail, the aromatic group does not form a stable hydrogen bond with the sulfoxide due to solvation of both the donor and acceptor by water. Hydrogen bonding may further enhance the interaction in hydrophobic and aprotic environments, however we do not observe that in our two test cases where the motif is solvent exposed. In LTá-TNFR1 and CaM, we have shown that competing interactions between methionine sulfoxide and nearby aromatic residues contributes to the modulation of protein structure and function.

To conclude, non-covalent interactions are the cornerstone of biological molecular recognition events. For bioactive small-molecule development, which exploits these interactions, sulfur is the third most commonly incorporated heteroatom in pharmaceuticals next to nitrogen and oxygen.[32] The sulfoxide-aromatic interaction provides a new handle for tuning affinities of small molecules for chemical probe and therapeutic development as well as altering protein function. Moreover, the dynamic nature of methionine oxidation provides a reversible switch that can be employed for introducing responsive molecules to changes in redox environment. The energy range of these altered interactions corresponds to twofold to tenfold change in the equilibrium constant, which together with the ambivalent character of sulfoxide functional groups, the dynamic nature of their formation, and their prevalence in biology and pharmaceutics, offers medicinal chemists and chemical biology a useful tool to probe biological systems.

Online Methods

Methods

Structural bioinformatics analysis of the Protein Data Bank—We analyzed a non-redundant subset of the PDB comprised of all structures containing at least one DMSO molecule using the Biopython toolset and a custom Python script adapted from our previous study[1]. Structures sharing >90% sequence identity were represented by a single structure with the highest score as ranked according to RCSB PDB quality factor algorithm. Redundant structures were excluded, as they do not represent truly independent data points for the purposes of our informatics study. Distances were defined between the DMSO sulfur and the center of the aromatic ring. Distance data were collected up to a cutoff of 20 Å. Hydrogen bonds were defined as having a heavy-atom donor to sulfonyl oxygen distance of < 3.5 Å. For the radial density function (RDF), the distances from each DMSO to aromatic groups were binned and the histogram normalized by shell volume. Each RDF was normalized by the relative population of amino acids in the analyzed PDB files (divided by 9.25% for F, Y, W, 22.47% for L, I, V, and by 100% for all amino acids). The resulting plots were normalized by the mean value at the long distance, non-interacting region of the “All Amino Acids” RDF to shift the bulk density to 1 and to cast the y-axis as an enrichment factor.

Structural bioinformatics analysis of the Cambridge Structural Database—Searches were executed in the Conquest program of the Cambridge Structural Database (CSD version 5.35, 2014 release), and structural analyses were performed using the Mercury program (v 1.5). The distance was defined as in the PDB. C-CH_2-C was used as a non-interacting analog to C-S-C, following a previous CSD analysis[2] The sulfur (or carbon in control) atom to aromatic distance was constrained to 0–10 Å. For the radial density function (RDF), the distances from each DMSO (or C-CH_2-C) to all aromatic groups were binned and divided by shell volume, then normalized by the total number of contacts. The resulting RDFs were shifted to 1 as in the PDB analysis, by normalizing to the value at the flat region of the C-CH_2-C RDF. A total of 20630 DMSO-aromatic pairs were found in 840 structures and 3093875 C-CH_2-C-aromatic pairs were found in 72745 structures.

ABF simulations of DMSO and aromatic groups in three solvents—Simulations were performed using the Adaptive Biasing Force (ABF) module in NAMD 2.9 using the CHARMM 36 generalized forcefield. The adaptive biasing force (ABF) module was used so that the system could overcome free energy barriers and fully sample all conformational states. Parameters for DMS were adapted from those for ethylmethylsulfide. The distance between the DMSO thioether and the center of mass of the 6-membered ring of phenol, or indole was used as the reaction coordinate of the mean force calculation. The system potential along the reaction coordinate was negated by the adaptive biasing force to simulate a flat free energy landscape. Each system was solvated in a ~45 $Å^3$ periodic box of TIP3P water, hexane, or ethyl acetate, for a total of 18 systems. The adaptive biasing potential was applied between 2.5 and 14 Å with a binwidth of 0.1 Å and simulations were carried out for at least 7.5×10^6 steps. All other simulation parameters were set as in our traditional MD (see Molecular dynamics simulations of LTα and TNFR1 methods). Supplementary Table 4 shows the effects of solvation on the calculated interaction energy between DMS/DMSO and each aromatic compound. The calculated PMF was not used in our analysis. Supplementary Figure 17 shows the distance between the aromatic ring and each heavy atom of the DMSO molecule and demonstrates no strong bias for the methyl groups to interact with the aromatic ring.

Peptide Synthesis—To study the appropriate pair sequences in a peptide chain, the un-oxidized amino acid Met or oxidized Met was inserted into the sequence: a) Tyr-Gly-Gly-Ser-Ala-Ala-Glu-Ala-***Aromatic***-Ala-Lys-Ala-**Met**-Ala-Arg-NH2, b) Tyr-Gly-Gly-Ser-Ala-Ala-Glu-Ala-***Aromatic***-Ala-Lys-Ala-**Met (ox)**-Ala-Arg-NH2. The peptides were assembled on Fmoc-PAL-PEG-PS resin by Fmoc chemistry using a PE Biosystems PioneerTM protein synthesis system. Single Met oxidation was accomplished by incorporation of Fmoc-Met (ox)-OH during synthesis. Standard *N*-[(dimethylamino)-1*H*-1,2,3-triazolo[4,5-*b*]pyridin-1-ylmethylene]-*N*-methylmethanaminium hexafluorophosphate N-oxide (HA TU)/ *N,N*-diisopropylethylamine (DIEA) (1/2.4 eq.) activation, in 1-methyl-2-pyrrolidinone (NMP), was applied. Fmoc deprotection was achieved with 20% piperidine in NMP. The final release of the peptides, with removal of the side chain protecting groups, were accomplished by exposure of the peptide-resin to 82.5% trifluoroacetic acid (TFA), 5% phenol, 5% thioanisol, 2.5% 1,2-ethanedithiol, 5% water (Reagent K). The peptides were precipitated with cold methyl-*t*-butyl ether, vortexed, centrifuged, decanted, and dried over argon. The dried peptides were dissolved in degassed water and purified by high-performance liquid chromatography (HPLC) using a reversed- phase C8 HPLC column. Peptide elution was achieved with a linear gradient from 0 to 34% B (95% acetonitrile / 5% water / 0.1% TFA) in 40 min at a flow rate of 2.5 mL/min with detection at 280 nm using a System Gold Beckman Coulter system. The HPLC fractions were collected and analyzed by mass spectrometry (MS).

Peptide Scaffold Design—The peptide scaffold utilized for defining the energetic impact of oxidation on Met-Aromatic interaction had a number of specific design elements. The helical content was optimized to reside within a range that enabled sensitive detection of its change by CD. The capping box motif at the N-terminus is the sequence Ser/Thr-X-X-Glu/Gln and is a helix stop signal[33]. This stop signal has Ser or Thr as the N-cap and a Glu

or Gln residue at position i+3, specifically; the sequence Ser-Ala-Ala-Glu is the capping motif in each of the peptides of the double mutant cycle. To this capping box, the N-terminus had a tyrosine added for concentration determination. The C-terminus was blocked by changing the COO- to a CONH2 to mediate this effect of dipole destabilization and to increase helical propensity[34].

Electrospray ionization (ESI)-MS—The peptides were analyzed on a LC/MSD ion trap (Agilent). ESI-MS spectra were acquired in positive ion mode. The solvent contained 40 % acetonitrile and 0.1 % formic acid. 10 to 30 μL sample were directly injected at a flow rate of 10 μL/min with a source temperature of 300 °C. The applied spray voltage was 3500 V, and the skimmer voltage 40 V. MS scans were acquired over an m/z range of 200 to 2000. The scan for the native mass 1499.69 Da of the sequence Tyr-Gly-Gly-Ser-Ala-Ala-Glu-Ala-**Phe**-Ala-Lys-Ala-**Met**-Ala-Arg, shows the single charged ion with *m/z* 1500.0 and the double charged ion *m/z* 750.7. The scan for the Met(O)-Phe sequence pair (1515.69 Da) shows the singly charged ion with *m/z* 1515.7, the double charged ion *m/z* 758.4, and the triple charged ion *m/z* 505.9. The observed masses for the respective molecular ions agree with the theoretical peptide scaffold design.

Circular Dichroism Spectroscopy—All peptides were stored in tetrafluoroethylene (TFE) after synthesis, which was removed by evaporation using Nitrogen gas prior to use. To ensure complete removal of the TFE, the sample was then put under vacuum for one hour. The dried peptide was re-constituted in 10mM KH_2PO_4, 100mM KCl at pH 7.5, and prepared for CD data collection. All CD experiments were performed on a Jasco J-815 CD Specrometer (Annapolis, MD) using a 0.1cm quartz cuvette at ~150μM peptide concentration. Concentrations of the peptide samples were determined using a Nanodrop Spectrometer. To display helical content and the presence of an isodichroic point ellipticity was measured between 200nm to 260 nm in 1nm increments from −2°C to 60°C for a FM, FM (ox), FA, AM, AM (ox) and AA. Once these characteristics were established for each construct, one data point was collected at 222nm at each 0.5°C or 2°C change as temperature increased from −2°C to 60°C. Cooling melts were also collected, recording the signal at 222nm, on all peptides as temperature decreased from 60°C to −2°C. All collected data points were averaged from 3 acquisitions of the recorded ellipticity.

Analysis of CD data—To extract the free energy of interaction from the temperature dependence of the CD, spectra were collected from the lowest experimentally accessible temperature (−2°C) to a temperature beyond which there were no observable changes in spectral shape for all peptides (60°C). The spectra are given in Supplementary Figure 7. Following Greenfield[18], we used the signal, Θ, at 222nm to report on changes in peptide structure. This wavelength was chosen because it reflects helical content and is also the wavelength at which the overall change in ellipticity is greatest across the temperature ramp. Following the same rationale we used previously[35], the CD signal is given by:

$$\Theta=(\Theta_{\text{initia}}+K\Theta_{\text{final}})/(1+K) \quad (3)$$

where $\Theta_{initial}$ is the value at 222nm recorded at −2°C, and Θ_{final} is the value at 222nm recorded at 60°C. Because $K = e^{-\Delta G/RT}$, we rewrite this equation as:

$$\Theta(T)=(\Theta_{\text{initial}}+e^{-\frac{\Delta G}{\text{RT}}}\Theta_{\text{final}})/(1+e^{-\frac{\Delta G}{\text{RT}}}), \quad (4)$$

We then fit the temperature dependent data, $\Theta(T)$, by substituting the Gibbs-Helmholtz equation into equation 4,

$$\Delta G=\Delta H_{\text{Tm}}\left(1-\frac{T}{T_m}\right)+\Delta C_p(T-T_m-T\left(\ln(\frac{T}{T_m})\right)), \quad (5)$$

and varying the three parameters: enthalpy (ΔH_{Tm}), heat capacity change (ΔC_p), and transition temperature (T_m).

Data for Phe-Met and Pet-Met(ox) are given for each replica in Supplementary Figure 5. By varying the concentrations of the peptide in each of its three replicates, the measured signal varies for each replica. The three replicates are globally fit simultaneously, an approach that improves the stringency of the parameter fits for each peptide. The free energy is then extracted from the fit at the desired temperature (T=0°C in this case). The change in free energy for each leg of the double mutant cycle is reported in Supplementary Figure 6.

Double Mutant Cycle—To construct a double mutant cycle, peptides were synthesized in which the aromatic residue and Met (or Met^{Ox}) was replaced first individually, then concurrently by the neutral residue alanine (Ala). The difference in ΔG between the Met-aromatic (oxidized or un-oxidized) and its respective singly substituted construct, or between the singly substituted construct and the doubly mutated construct gives a ΔΔG. The difference of the respective ΔΔG values produces a ΔΔΔG, which indicates whether the specific interaction is contributing to the stabilization of structure. ΔΔΔG is simplified here as ΔG_{int} to match the free energy of interaction reported in the reference[7] (the two expressions are thermodynamically equivalent, although the cited study did not use a double mutant cycle). If ΔG_{int} equals zero, the interaction observed is not contributing to the structural stability; if greater than zero, the interaction is stabilizing; and if less than zero, destabilizing[36–38].

Principal Component Analysis—Principal component analysis for each of the FM, FM^{Ox}, FA, AM, AM^{Ox}, and AA peptides data sets was carried out with the “prcomp” function of the program R (v. 3.2.1). For each data set only one of the three replicates was used. To increase the sensitivity of the analysis, we focused on the isodichroic point region by analyzing only the wavelengths between 200 nm and 210 nm (11 data points), while the entire temperature range was included in the analysis. The correlation matrix was calculated between the mean-centered vectors of wavelengths:

$$\text{C\_ ij}=\text{T\_ i}(\lambda\_\ 1,\lambda\_\ 2,\ldots,\lambda\_\ \text{N})\cdot\text{T\_ j}(\lambda\_\ 1,\lambda\_\ 2,\ldots,\lambda\_\ \text{N})$$

The results reported in Supplementary Figure 9 and Supplementary Table 5 show that the first two principal components describe 94% or more of the total variance, which is consistent with the assumption that the change in molar ellipticity is dominated by only two sources of signal.

NMR Experiments—Concentrations of peptide samples were obtained using ultraviolet absorbance of Tyrosine (ε= 1450) in 8 M urea. Peptide Y-Met^{Ox} (YGGSAAEAFAKAM(ox)AR-NH_2) was dissolved in deuterated methanol (3 mM). F-Met^{Ox} (YGGSAAEAFAKAM(ox)AR-NH_2) was dissolved in acidic (pH 3.5) D_2O, taken at 4°C. ^1H-^1H ROESY experiments (mixing time = 200 ms) were performed on a Bruker 700 MHz spectrometer with a CryoProbe: 5 mm TXI probe of Z-Gradient. ^1H experiments comparing control peptide, A-Met^{Ox} to F-Met^{Ox} in MeOD were performed on a Bruker Advance III HD 500 MHz instrument with a 5 mm Prodigy TCI cryoprobe with z-axis gradients. Data was processed and analyzed using Bruker Topspin 3.2.

Dipolar EPR spectroscopy of spin-labeled calmodulin—A mammalian CaM mutant, with V136 and T146 both mutated to Cys, was prepared by site-directed mutagenesis (QuikChange II kit, Agilent, Santa Clara CA), confirmed by DNA sequencing, expressed and purified as described previously[39], and dialyzed overnight at 4°C against 10mM NaCl, 10mM Tris (pH 7.0). Spin-labeling with maleimide spin label (MSL, N-(1-oxyl-2,2,5,5-tetramethyl pyrrolidinyl) maleimide, Toronto Research Chemicals, Canada) was carried out by incubating 120 μM CaM with 480 μM MSL in CaM buffer (10 mM NaCl, 10 mM Tris, 5 mM EGTA, pH 7.0) for two hours at 22° C (followed by overnight dialysis against CaM buffer to remove unreacted label), resulting in complete labeling of the two Cys, as shown by mass spectrometry. To oxidize methionine side chains, spin-labeled CaM was incubated in 500 mM hydrogen peroxide for 30 min, followed by dialysis into CaM buffer. As shown previously under similar conditions[39], mass spectrometry verified that all of the nine methionine residues of CaM were oxidized. X-band (9.5 GHz) EPR spectra of 200 μM CaM (in CaM buffer plus 10% glycerol) were acquired at 200° K with a Bruker ER500 spectrometer, using 1 G modulation amplitude and sub-saturating microwave power (0.63 mW). EPR spectra were analyzed to determine the distribution of distances between the two spin labels, as described previously[40].

Ligand preparation and treatment—Plasmids encoding human LTα and human TNF expressing an N-terminal FLAG tag, downstream from an inducible T7 promoter were subcloned using standard cloning techniques. Plasmids were transformed into chemically competent BL21 bacteria, plated on LB agar plates, and cultured in LB to an OD600 of ~0.5. Cultures were then cooled to 18°C, induced with 0.5 mM isopropyl β-D-1-thiogalactopyranoside, and grown for 18 hours. The bacteria suspension was centrifuged, then lysed by sonication in ice-cold PBS. The lysate was column purified using anti-FLAG M2 Affinity Gel (Sigma) according to the manufacturer protocol, dialyzed exhaustively against MilliQ H_2O, and then lyophilized. FLAG-LTα, as prepared in our laboratory, contains 4 methionine residues, of which M120 and M133 potentially play structural and functional roles in the ligand-receptor complex. M133 is buried between two folds of a β-sheet, and its precise functional role, if any, has not been established. For the LTα-M120

mutant, we mutated M133 to valine and M20 to alanine in order to match the homologous residues found in Bos Taurus LTα, which shares 73% sequence identity and 81% sequence similarity (Sequence Manipulation Suite), but lacks methionines except for its N-terminus. TNF, which also binds to and activates TNFR1 with similar potency[41] was used as a control.

Oxidative stress was applied by dissolving 8 μg of ligand in buffer containing 10 mM HEPES, 100 mM KCl, 1 mM MgCl, 1 mM CaCl, then adding 100 mM H_2O_2 to a total volume of 100 uL. The oxidation reaction was allowed to proceed for 18 hours at room temperature, then stopped by removing H_2O_2 in 2 sequential stages using Zeba 7KDa molecular weight cutoff spin columns. Removal of H_2O_2 was confirmed by Amplex red assay, and the residual concentration of H_2O_2 was determined as insufficient to induce autophagy. We measured tryptophan fluorescence to confirm that oxidation does not lead to gross unfolding of LTα, finding no shift in the emission spectrum when excited at 280 nm (Supplementary Figure 15).

Western blot analysis of IκBα—HEK 293 cells were maintained in DMEM supplemented with 10% FBS, penicillin/streptomycin, and 2 mM L-glutamine. Confluent cells were split at 1:12 into 6-well plates and used for experiments on day 3. Untreated and oxidized ligands were added to cells to final concentrations of 200 ng/mL and 20 ng/mL for LTα and TNF respectively, and incubated for 20 minutes at 37 °C. Cells were then washed once and gently sheared from the plate with ice-cold PBS, then centrifuged and resuspended in radioimmunoprecipitation assay (RIPA) lysis buffer. Cell lysates were normalized to equal protein concentrations, and 60 μg were loaded onto 4–12% Bis-Tris gradient gels for Western blot analysis. IκBα was detected using horseradish peroxidase (HRP) conjugated rabbit α-IκBα (Cell Signaling Technology, #9242, 1:1000) and α-Rabbit IgG (Amersham, 1:10,000). Full gels are shown in Supplementary Fig. 16.

Co-immunoprecipitation—Co-immunoprecipitation was performed using anti-FLAG M2 agarose beads (Invitrogen) according to the manufacturer instructions. Briefly, HEK 293 cells were split at 1:12 into 15 cm plates and transfected with 8 μg of plasmid encoding TNFR1 (pCMV6-XL5-TNFR1) on day 1 by calcium phosphate transfection. On day 3, cells were lifted by shearing, washed once, and resuspended in ice-cold PBS at ~10^6/mL. LTα and TNF were added at 12 and 25 ng/mL respectively, and the cells were incubated for 30 minutes at 4 °C while rocking. Cells were then washed 3 times in ice-cold PBS and resuspended in RIPA lysis buffer, then analyzed by Western blot. TNFR1 was detected using rabbit α-TNFR1 (Abcam, ab19139, 1:1000) and α-rabbit secondary, as described above. Full gels are shown in Supplementary Fig. 16.

Quantum calculations—The interaction energy between model compounds was investigated with quantum mechanical calculations performed in the gas phase. The reduced and oxidized states of methionine were modeled by dimethyl sulfide (DMS) and dimethyl sulfoxide (DMSO), respectively; the side chains of phenylalanine, tyrosine, and tryptophan were modeled by benzene, phenol, and indole. The interaction energy between compounds A and B was defined as:

$$E(\mathrm{AB})_{\mathrm{int}} = E(\mathrm{AB})_{\mathrm{complex}} - E(A) - E(B) \quad (1)$$

All energies were obtained from fully unrestrained structure optimizations carried out with Gaussian 09[42] using the Møller-Plesset perturbation theory at the second order (MP2/6–311+G(d,p)) and account for basis set superposition error[43]. Additional data computed at the M06–2X/6–311+G(d,p)[44] level are reported in Supplementary Table 1. These two levels of calculation were chosen because we previously showed that they bracket the interaction energy calculated at the CCSD(T)/6–311+G(d,p) level[1]. Notice that for each complex several minima were characterized, and the data is reported only for the lowest energy one.

The dispersion energy contribution to the complex formation was calculated as in Ref. [1] by taking the difference between the interaction energy (eq 1) computed at the MP2 and Hartree-Fock (HF) levels. In both cases the same basis set was employed, and the HF energies were calculated as single point on the MP2 optimized structures.

The effect that the variety of conformations adopted in solution has on the interaction energy was investigated by averaging the interaction energies of 128 structures randomly sampled from the minimum (sulfur – aromatic distance between 4 – 6 Å) of the ABF simulations in ethyl acetate described above. Hydrogen bonded structures were defined as having donor-acceptor distance of <2.5 Å and not-hydrogen bonded structures had a donor-acceptor distance of >4 Å. Upon removal of the solvent, the instantaneous interaction energy was calculated at the MP2/aug-cc-pVDZ level using eq. 1 without any additional structure optimization.

A similar procedure was employed to investigate the interaction energy between the side chains of M120, Y96, and Y122 in LTα. From the MD simulations described below, 128 structures were randomly selected and the average interaction energy calculated at the MP2/aug-cc-pVDZ level as:

$$E(M_{120}Y_{96}Y_{122})_{\mathrm{int}} = E(M_{120}Y_{96}Y_{122})_{\mathrm{complex}} - E(M_{120}) - E(Y_{96}) - E(Y_{122}) \quad (2)$$

The side chains were truncated at the C_β-C_γ bond and the missing valence was saturated with a hydrogen atom. Upon removal of the rest of the protein and the solvent and without any further optimization, the interaction energy was calculated at the MP2/aug-cc-pVDZ level and corrected for the basis set superposition error.

For the calculations on the ethyl acetate simulations described above, the Natural Bond Orbital[45] (NBO) charges were calculated and averaged over all 128 structures. The NBO localization scheme was tested along Mulliken[46] localization over a number of different basis sets of increasing size. Because the results showed a strong dependence of the Mulliken charges on the basis set size[47] while NBO charges did not, the NBO localization scheme was preferred.

Replica exchange molecular dynamics of calmodulin—The replica exchange molecular dynamics (REMD) simulation was performed in NAMD 2.9 using the CHARMM22 potential parameters[48]. Eleven residues of the last helix (136–146) of CaM (3CLN.pdb)[27] were used in the all-atom point-charge force field *in vacuo* to match conditions of the quantum calculations. Eight replicas with temperatures exponentially spaced from 300K to 600K (300, 331.23, 365.7, 403.77, 445.8, 492.2, 543.43, 600 K) were used with the initial velocities of the atoms generated by the Maxwell-Boltzmann distribution and a timestep of 1 fs. The first 10^6 steps were performed without attempting exchanges to equilibrate, then exchanges were attempted every 1000 steps (1 ps) with an acceptance rate ~20%. Coordinates were taken every 100,000 steps (100 ps). 78,810 frames were taken for the unoxidized peptide and 74,400 frames for the oxidized peptide, corresponding to a total simulation time per replica of 985 and 930 ns, respectively. Only the replicas at 300 K were used in the analysis. Methionine-aromatic interactions were identified as having a distance of <7 Å and an angle less than 60°, consistent with previous definitions[1,2]. Hydrogen bonds were cutoff at <2.5Å from hydrogen to acceptor.

Molecular dynamics simulations of LTα and TNFR1—We carried out molecular dynamics simulations of oxidized or unoxidized LTα in its unbound state and unoxidized in complex with TNFR1 using the structure, 1TNR as the starting configuration[49]. Two additional systems, a Y122 interacting configuration and a Y96 interacting configuration, were constructed in which M120 began bound to Y122 or Y96, respectively, while all other residues in the 1TNR crystal structure were left essentially unchanged (minor manipulation and steepest descent minimization was required to resolve overlap in the binding pocket). The starting configurations of M120, Y96, and Y122 in these systems were taken from the oxidized ligand simulation. Each system was solvated in a box of at least 40,000 explicit water molecules modeled as TIP3P in order to fully capture solvation effects [50] and the charge was neutralized by adding K^+ and Cl^- ions. The isothermal-isobaric (NPT) ensemble was used along with the CHARMM36 force field[51–53] at a temperature of 303 K and 1 atm pressure, which were maintained using the Langevin piston and Nosé-Hoover[54] algorithms. Parameters for Met^{Ox} were provided by Krzysztof Kuczera[55] and adapted for use in the CHARMM36 force field. Long-range electrostatics were calculated using the particle mesh Ewald method [56] with a 1.5 Å grid spacing and 4th order interpolation. Lennard-Jones interactions were switched off at a cutoff distance of 10 Å. Each system (except the Y96 and Y122 interacting configurations) was minimized using NAMD 2.8[48] for 1000 steps, then equilibrated with Cα harmonic constraints of 1, 0.1, and 0.01 kcal/mol/Å^2 for 2 ns at each stage. Dynamic trajectories were propagated with the r-RESPA algorithm [57] with a 2 fs time step and the RATTLE algorithm [58] was applied to all covalent bonds involving hydrogen. The ligand-receptor system was simulated for ~35 ns and distance and angle analyses were averaged over the entire trajectory. The ligand-only systems were simulated for a total of ~430 ns. The first 150 ns (including relaxation) were excluded from structural analyses to allow re-equilibration of the ligand after removal of the receptor chains. The Y96 and Y122 interacting systems were equilibrated with great care before running unrestrained dynamics. Each was minimized to resolve steric clashes, then equilibrated according to the scheme shown in Supplementary Table 6. Distances and angles were calculated from the thioether

sulfur of M120 to the centers and normal vectors of the aromatic groups of Y96, Y122, and W107. Methionine-aromatic interaction cutoffs were defined as in the CaM simulations.

Supplementary Material

Refer to Web version on PubMed Central for supplementary material.

Acknowledgments

This work was supported by grants to J.N.S. (NIH R01 GM107175), D.D.T. (NIH R37 AG26160), W.C.K.P (NSF-CAREER CHE-1352091) and A.H. (NSF-CAREER MCB-0845676). This work was carried out in part using computing resources at the University of Minnesota Supercomputing Institute. EPR, and CD experiments were performed at the Biophysical Spectroscopy Center, University of Minnesota. We thank John Evans for discussion and guidance regarding the principal component analysis of our CD data.

References

1. Valley CC, et al. The Methionine-aromatic Motif Plays a Unique Role in Stabilizing Protein Structure. J Biol Chem. 2012; 287:34979–34991. [PubMed: 22859300]
2. Zauhar RJ, Colbert CL, Morgan RS, Welsh WJ. Evidence for a strong sulfur-aromatic interaction derived from crystallographic data. Biopolymers. 2000; 53:233–248. [PubMed: 10679628]
3. Reid KSC, Lindley PF, Thornton JM. Sulphur-aromatic interactions in proteins. FEBS Letters. 1985; 190:209–213.
4. Pranata J. Sulfur-Aromatic Interactions: A Computational Study of the Dimethyl Sulfide-Benzene Complex. Bioorganic Chemistry. 1997; 25:213–219.
5. Morgan RS, McAdon JM. Predictor for sulfur-aromatic interactions in globular proteins. International journal of peptide and protein research. 1980; 15:177–180. [PubMed: 7372409]
6. Morgan RS, Tatsch CE, Gushard RH, McAdon J, Warme PK. Chains of alternating sulfur and pi-bonded atoms in eight small proteins. International journal of peptide and protein research. 1978; 11:209–217. [PubMed: 206519]
7. Viguera AR, Serrano L. Side-chain interactions between sulfur-containing amino acids and phenylalanine in α-helices. Biochemistry. 1995; 34:8771–8779. [PubMed: 7612617]
8. Shechter Y, Burstein Y, Patchornik A. Selective oxidation of methionine residues in proteins. Biochemistry. 1975; 14:4497–4503. [PubMed: 1174512]
9. Hoshi T, Heinemann SH. Regulation of cell function by methionine oxidation and reduction. Journal of Physiology-London. 2001; 531:1–11.
10. Levine RL, Berlett BS, Moskovitz J, Mosoni L, Stadtman ER. Methionine residues may protect proteins from critical oxidative damage. Mech Ageing Dev. 1999; 107:323–332. [PubMed: 10360685]
11. Kim G, Weiss SJ, Levine RL. Methionine oxidation and reduction in proteins. Biochimica et biophysica acta. 2014; 1840:901–905. [PubMed: 23648414]
12. Arakawa T, Kita Y, Timasheff SN. Protein precipitation and denaturation by dimethyl sulfoxide. Biophysical Chemistry. 2007; 131:62–70. [PubMed: 17904724]
13. Rose GD, Geselowitz AR, Lesser GJ, Lee RH, Zehfus MH. HYDROPHOBICITY OF AMINO-ACID RESIDUES IN GLOBULAR-PROTEINS. Science. 1985; 229:834–838. [PubMed: 4023714]
14. Dougherty DA. Cation-pi interactions in chemistry and biology: a new view of benzene, Phe, Tyr, and Trp. Science. 1996; 271:163–168. [PubMed: 8539615]
15. Bogan AA, Thorn KS. Anatomy of hot spots in protein interfaces. Journal of Molecular Biology. 1998; 280:1–9. [PubMed: 9653027]
16. Gottlieb HE, Kotlyar V, Nudelman A. NMR Chemical Shifts of Common Laboratory Solvents as Trace Impurities. J Org Chem. 1997; 62:7512–7515. [PubMed: 11671879]

17. Butterfield SM, Patel PR, Waters ML. Contribution of aromatic interactions to alpha-helix stability. J Am Chem Soc. 2002; 124:9751–9755. [PubMed: 12175233]
18. Greenfield NJ. Using circular dichroism collected as a function of temperature to determine the thermodynamics of protein unfolding and binding interactions. Nat Protoc. 2006; 1:2527–2535. [PubMed: 17406506]
19. Marqusee S, Baldwin RL. Helix stabilization by Glu-…Lys+ salt bridges in short peptides of de novo design. Proc Natl Acad Sci U S A. 1987; 84:8898–8902. [PubMed: 3122208]
20. Pearson KL III. On lines and planes of closest fit to systems of points in space. The London, Edinburgh, and Dublin Philosophical Magazine and Journal of Science. 1901; 2:559–572.
21. Yin D, Kuczera K, Squier TC. The sensitivity of carboxyl-terminal methionines in calmodulin isoforms to oxidation by H(2)O(2) modulates the ability to activate the plasma membrane Ca-ATPase. Chemical research in toxicology. 2000; 13:103–110. [PubMed: 10688534]
22. Sacksteder CA, et al. Tertiary structural rearrangements upon oxidation of Methionine145 in calmodulin promotes targeted proteasomal degradation. Biophys J. 2006; 91:1480–1493. [PubMed: 16751245]
23. Gao J, Yao Y, Squier TC. Oxidatively modified calmodulin binds to the plasma membrane Ca-ATPase in a nonproductive and conformationally disordered complex. Biophys J. 2001; 80:1791–1801. [PubMed: 11259292]
24. Gao J, et al. Loss of conformational stability in calmodulin upon methionine oxidation. Biophysical journal. 1998; 74:1115–1134. [PubMed: 9512014]
25. Boschek CB, Jones TE, Smallwood HS, Squier TC, Bigelow DJ. Loss of the calmodulin-dependent inhibition of the RyR1 calcium release channel upon oxidation of methionines in calmodulin. Biochemistry. 2008; 47:131–142. [PubMed: 18076146]
26. Bartlett RK, et al. Oxidation of Met144 and Met145 in calmodulin blocks calmodulin dependent activation of the plasma membrane Ca-ATPase. Biochemistry. 2003; 42:3231–3238. [PubMed: 12641454]
27. Babu YS, Bugg CE, Cook WJ. Structure of calmodulin refined at 2.2 A resolution. J Mol Biol. 1988; 204:191–204. [PubMed: 3145979]
28. Kuboniwa H, et al. Solution structure of calcium-free calmodulin. Nat Struct Biol. 1995; 2:768–776. [PubMed: 7552748]
29. Mukherjea P, Maune JF, Beckingham K. Interlobe communication in multiple calcium-binding site mutants of Drosophila calmodulin. Protein Sci. 1996; 5:468–477. [PubMed: 8868483]
30. Anbanandam A, et al. Mediating molecular recognition by methionine oxidation: conformational switching by oxidation of methionine in the carboxyl-terminal domain of calmodulin. Biochemistry. 2005; 44:9486–9496. [PubMed: 15996103]
31. Jeschke G. DEER Distance Measurements on Proteins. Annual Review of Physical Chemistry, Vol 63. 2012; 63:419–446.
32. Ilardi EA, Vitaku E, Njardarson JT. Data-Mining for Sulfur and Fluorine: An Evaluation of Pharmaceuticals To Reveal Opportunities for Drug Design and Discovery. Journal of Medicinal Chemistry. 2014; 57:2832–2842. [PubMed: 24102067]

Methods-only references

33. Jimenez MA, Munoz V, Rico M, Serrano L. HELIX STOP AND START SIGNALS IN PEPTIDES AND PROTEINS - THE CAPPING BOX DOES NOT NECESSARILY PREVENT HELIX ELONGATION. Journal of Molecular Biology. 1994; 242:487–496. [PubMed: 7932705]
34. Vasquez M, Pincus MR, Scheraga HA. HELIX COIL TRANSITION THEORY INCLUDING LONG-RANGE ELECTROSTATIC INTERACTIONS - APPLICATION TO GLOBULAR-PROTEINS. Biopolymers. 1987; 26:351–371. [PubMed: 3567318]
35. Fealey ME, et al. Negative Coupling as a Mechanism for Signal Propagation between C2 Domains of Synaptotagmin I. Plos One. 2012; 7:11.
36. Horovitz A. Double-mutant cycles: A powerful tool for analyzing protein structure and function. Folding & Design. 1996; 1:R121–R126. [PubMed: 9080186]

37. Horovitz A, Serrano L, Avron B, Bycroft M, Fersht AR. STRENGTH AND COOPERATIVITY OF CONTRIBUTIONS OF SURFACE SALT BRIDGES TO PROTEIN STABILITY. Journal of Molecular Biology. 1990; 216:1031–1044. [PubMed: 2266554]
38. Serrano L, Bycroft M, Fersht AR. AROMATIC AROMATIC INTERACTIONS AND PROTEIN STABILITY - INVESTIGATION BY DOUBLE-MUTANT CYCLES. Journal of Molecular Biology. 1991; 218:465–475. [PubMed: 2010920]
39. Balog EM, Lockamy EL, Thomas DD, Ferrington DA. Site-specific methionine oxidation initiates calmodulin degradation by the 20S proteasome. Biochemistry. 2009; 48:3005–3016. [PubMed: 19231837]
40. Klein JC, et al. Actin-binding cleft closure in myosin II probed by site-directed spin labeling and pulsed EPR. Proceedings of the National Academy of Sciences of the United States of America. 2008; 105:12867–12872. [PubMed: 18725645]
41. Etemadi N, et al. Lymphotoxin α induces apoptosis, necroptosis and inflammatory signals with the same potency as tumour necrosis factor. FEBS J. 2013; 280:5283–5297. [PubMed: 23815148]
42. Frisch, MJ., et al. Gaussian 09, Revision D.01. Wallingford CT: 2009.
43. Boys SF, Bernardi F. The calculation of small molecular interactions by the differences of separate total energies. Some procedures with reduced errors. Molecular Physics. 1970; 19:553–566.
44. Zhao Y, Truhlar DG. A new local density functional for main-group thermochemistry, transition metal bonding, thermochemical kinetics, and noncovalent interactions. Journal of Chemical Physics. 2006; 125
45. Reed AE, Curtiss LA, Weinhold F. Intermolecular interactions from a natural bond orbital, donor-acceptor viewpoint. Chemical Reviews. 1988; 88:899–926.
46. Mulliken RS. Electronic Population Analysis on LCAO-MO Molecular Wave Functions. I. The Journal of Chemical Physics. 1955; 23:1833–1840.
47. Cramer, CJ. Essentials of computational chemistry: theories and models. John Wiley & Sons; 2013.
48. Phillips JC, et al. Scalable molecular dynamics with NAMD. J Comput Chem. 2005; 26:1781–1802. [PubMed: 16222654]
49. Banner DW, et al. Crystal structure of the soluble human 55 kd TNF receptor-human TNF beta complex: implications for TNF receptor activation. Cell. 1993; 73:431–445. [PubMed: 8387891]
50. Jorgensen WL, Chandrasekhar J, Madura JD, Impey RW, Klein ML. Comparison of Simple Potential Functions for Simulating Liquid Water. Journal of Chemical Physics. 1983; 79:926–935.
51. MacKerell AD, et al. All-atom empirical potential for molecular modeling and dynamics studies of proteins. Journal of Physical Chemistry B. 1998; 102:3586–3616.
52. MacKerell AD, Feig M, Brooks CL. Improved treatment of the protein backbone in empirical force fields. Journal of the American Chemical Society. 2004; 126:698–699. [PubMed: 14733527]
53. Best RB, et al. Optimization of the additive CHARMM all-atom protein force field targeting improved sampling of the backbone φ, ψ and side-chain χ(1) and χ(2) dihedral angles. J Chem Theory Comput. 2012; 8:3257–3273. [PubMed: 23341755]
54. Martyna GJ, Tobias DJ, Klein ML. Constant-Pressure Molecular-Dynamics Algorithms. Journal of Chemical Physics. 1994; 101:4177–4189.
55. Jas GS, Kuczera K. Free-energy simulations of the oxidation of C-terminal methionines in calmodulin. Proteins: Structure, Function and Genetics. 2002; 48:257–268.
56. Darden T, Perera L, Li LP, Pedersen L. New tricks for modelers from the crystallography toolkit: the particle mesh Ewald algorithm and its use in nucleic acid simulations. Structure with Folding & Design. 1999; 7:R55–R60. [PubMed: 10368306]
57. Tuckerman M, Berne BJ, Martyna GJ. Reversible Multiple Time Scale Molecular-Dynamics. Journal of Chemical Physics. 1992; 97:1990–2001.
58. Andersen HC. Rattle - a Velocity Version of the Shake Algorithm for Molecular-Dynamics Calculations. Journal of Computational Physics. 1983; 52:24–34.

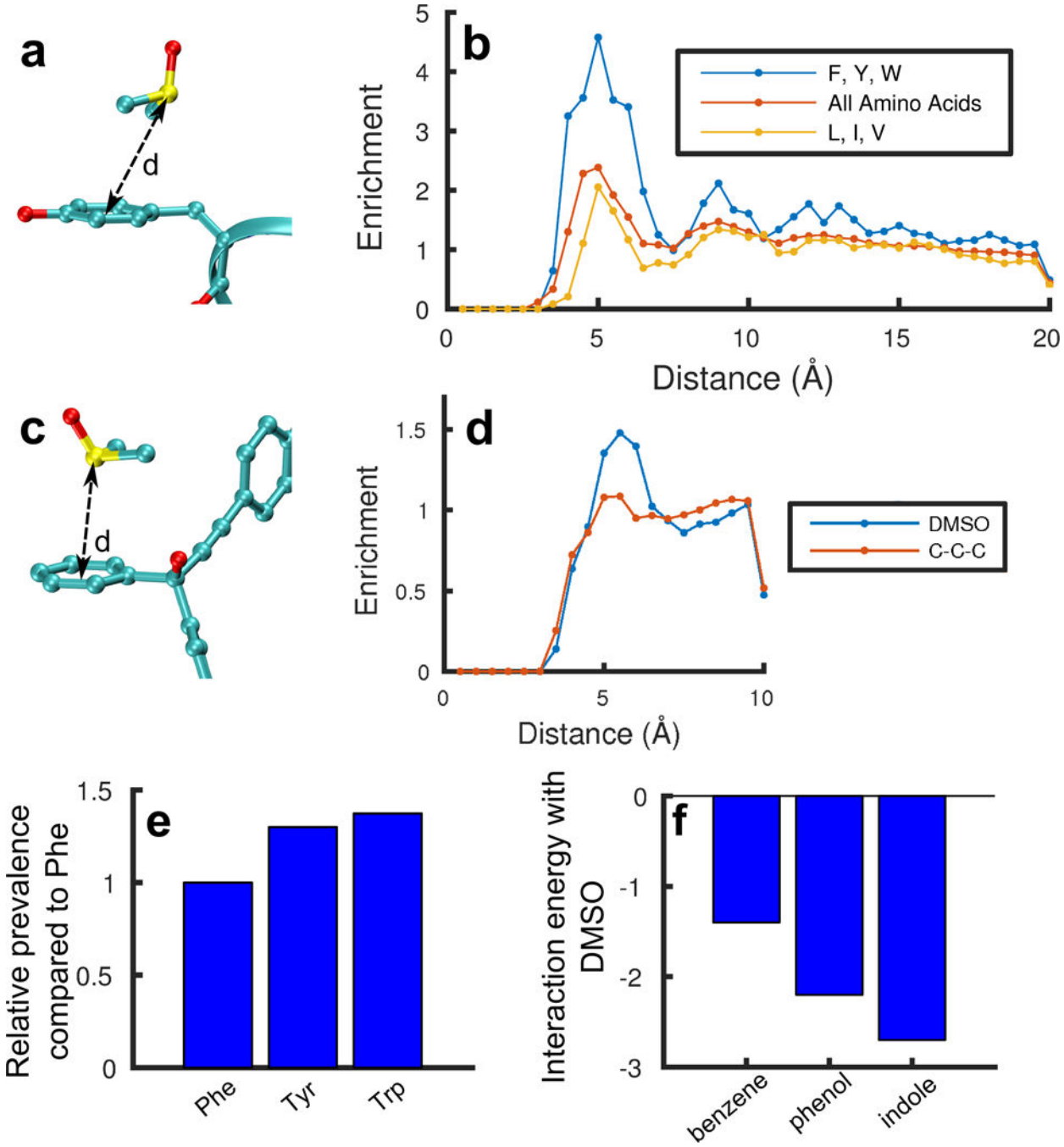

Figure 1. Structural informatics search of the CSD and PDB and interaction energy

A representative snapshot of a DMSO-aromatic interaction taken from the PDB (PDB: 4KAD) (a). The radial distributions of all amino acids and aromatic amino acids is plotted relative to DMSO, showing a clear enrichment of aromatic residues 4–7 Å from DMSO (b). We compare to the radial density of all amino acids and the aliphatic amino acids, Leu, Ile, and Val, relative to DMSO. A representative snapshot of a DMSO-aromatic interaction taken from the CSD (CSD: AWUHEF) (c). The radial density of aromatic groups relative to DMSO sulfur shows an enrichment around 4–7 Å (d). We compare to the radial density of

aromatic groups relative to C-CH_2-C motifs, which are non-interacting. Frequency of DMSO interactions with each aromatic amino acid are plotted. These values are normalized against the abundance of each aromatic group in the PDB subset analyzed and shows enrichment of interactions with tyrosine and tryptophan compared to DMSO-phenylalanine interactions (a). Interaction energies calculated at the MP2/6–311+G(d,p) with CP-corrections for the complexes between benzene, phenol, and indole and DMSO. The structures exclude hydrogen bonding and are calculated using ensembles of configurations from the simulations as described (b).

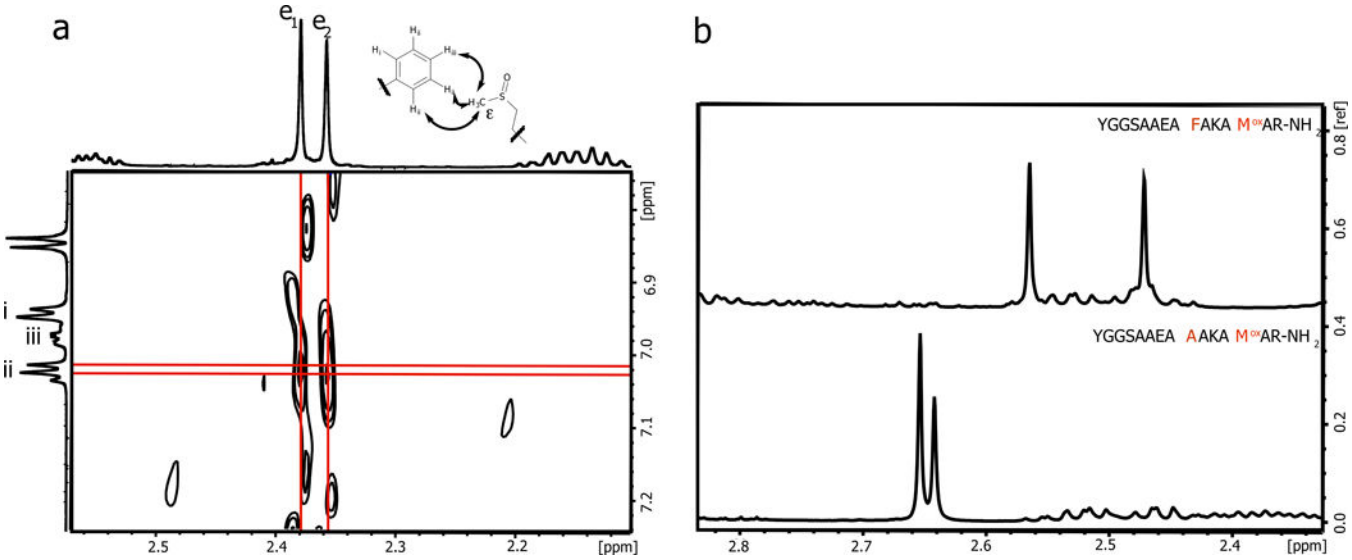

Figure 2. ^{1}H-^{1}H ROESY NMR and chemical shift analysis of α-helical peptide mixtures of two diasteriomers containing the *R* and *S* sulfoxide of methionine

^{1}H-^{1}H ROESY NMR correlating NOEs from the two diastereomeric ε-methyls of oxomethionine to the aromatic resonances of phenylalanine. The strongest NOEs correlating with the aryl protons of phenylalanine Hb, are indicated by thicker arrows (a). Comparative analysis of F-Met^{Ox} and A-Met^{Ox}^{1}H NMR experiments indicating an upfield shift of the ε-methyl resonances of oxomethionine when an aromatic ring is present relative to a methyl group (b).

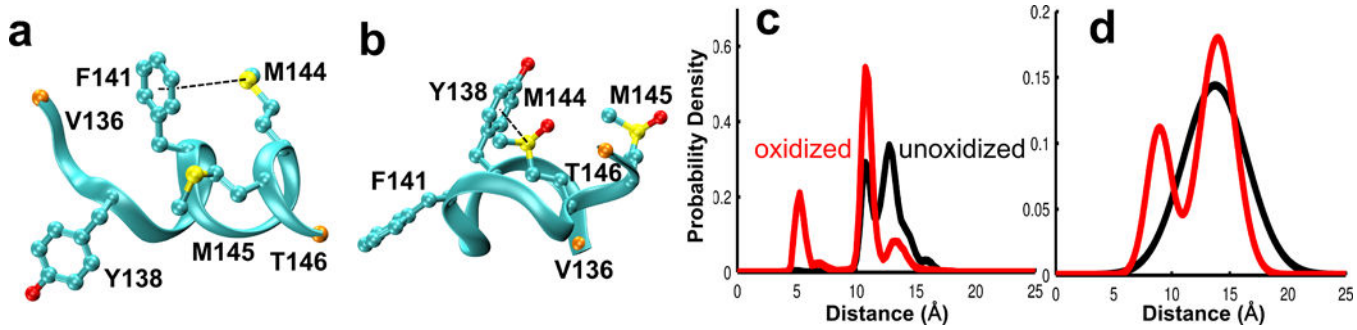

Figure 3. REMD and EPR measurements of CaM

Structure of unoxidized apo-CaM fragment (residue 136–146, PDB:1CFD) where F141 interacts with M144 (a) compared to a representative structure of the Y138 aromatic interacting with oxidized M144 (b) from REMD. Distance distribution calculated between Cα atoms of T136/V146 from REMD (c) and best-fit models of the distance distribution from dipolar EPR spectroscopy at submicromolar [Ca^{2+}] with maleimide spin labels at Cys residues 136 and 146 (d).

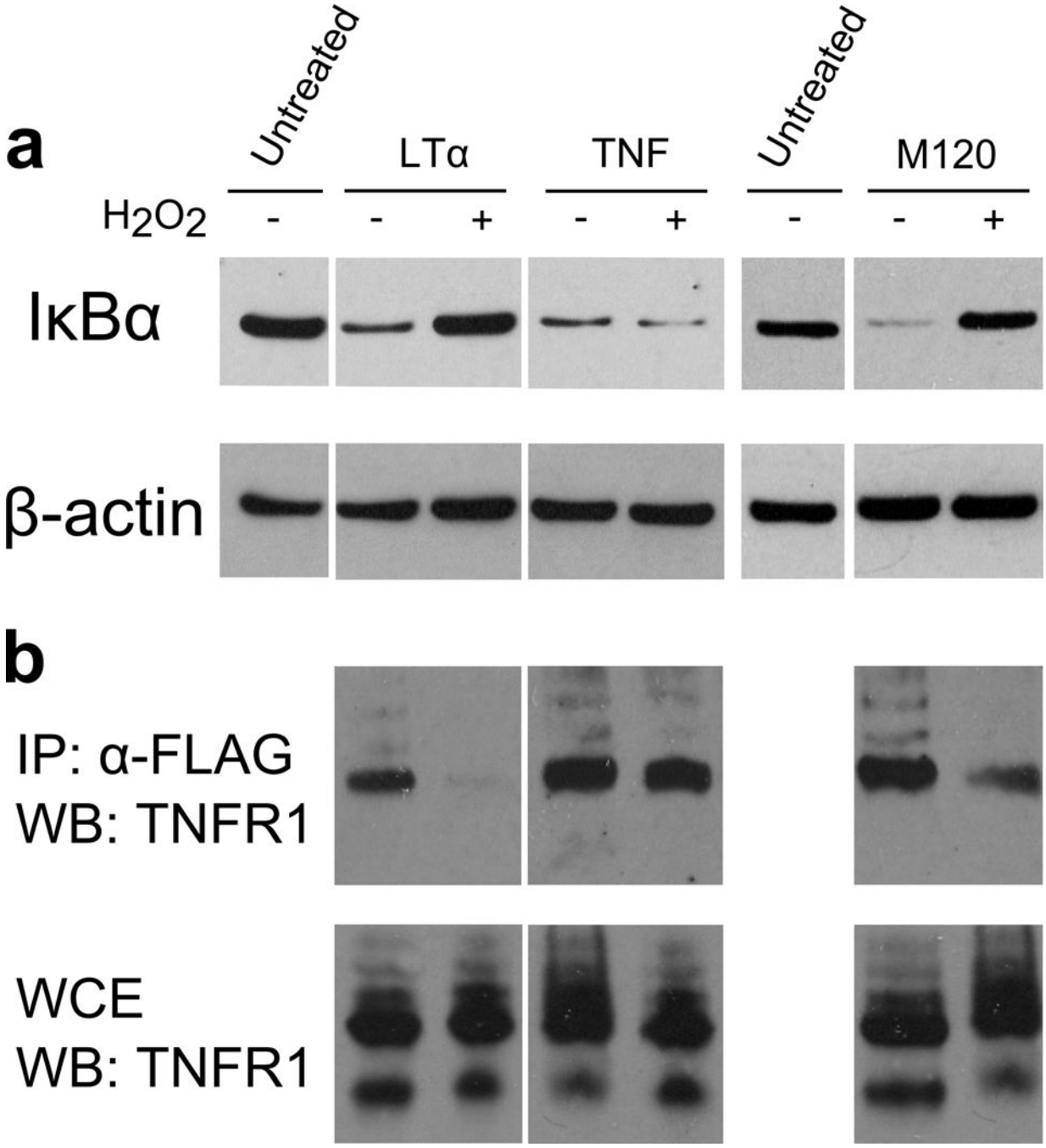

Figure 4. Oxidation of LTα, but not TNF ablates its interaction with TNFR1

Western blot analysis of IκBα degradation in response to treatment with oxidized (+) and unoxidized (−) LTα and TNF (a). LTα bioactivity is ablated after exposure to oxidative stress. This effect is not observed in TNF, where oxidized and unoxidized ligand trigger IκBα degradation to the same extent. Exposure to oxidative stress similarly prevented M120 LTα from triggering IκBα degradation. Co-immunoprecipitation of TNFR1 with oxidized (+) and unoxidized (−) ligands (b). LTα efficiently pulls down TNFR1 when untreated. Treatment of LTα under oxidative stress causes dramatic reduction in the amount of receptor

bound. TNF is again unaffected by oxidative stress. The LTα M120 mutant again behaves the same as wild-type, indicating that oxidation of M120 is responsible for the loss of binding. The Western Blots shown are representative of at least 2 independent experiments. Full gels are shown in Supplementary Fig. 16.

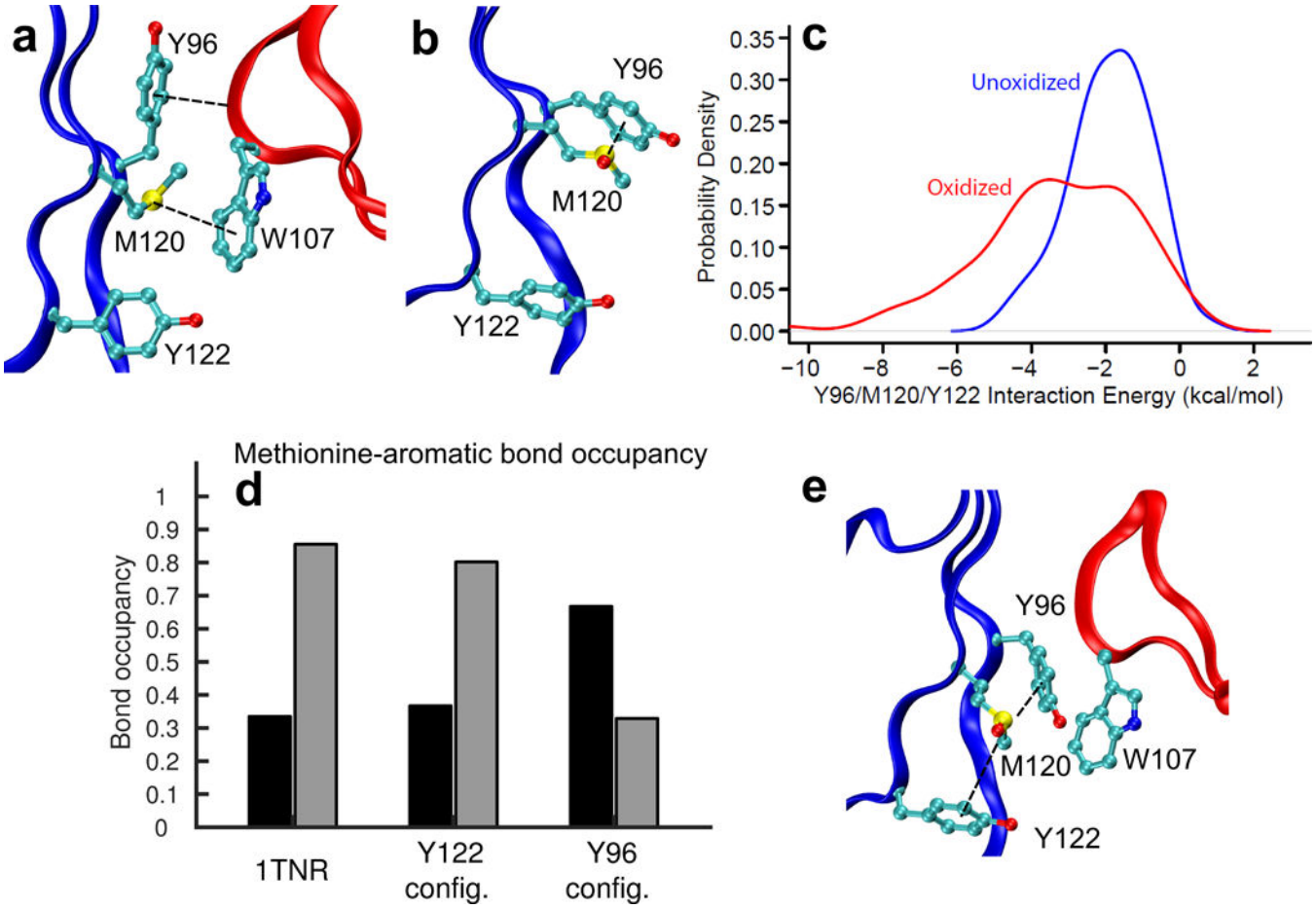

Figure 5. Molecular dynamics simulations of LTα with M120 oxidized show that competitive interaction of M120 with Y96/Y122 prevents its interaction with W107

In the receptor bound state, Y96 is folded upward so that it interacts with the backbone of the receptor, allowing M120 to form a stable methionine-aromatic interaction with W107 (a). When Met120 is oxidized, it draws Y96 downward so that it protrudes into the binding pocket (b). The histogram of the interaction energy between M120 and Y96/Y122 calculated from 128 structures taken from the MD simulations shows enhanced interaction due to oxidation. The histogram was smoothed with the Gaussian kernel-smoothing function "density" of the program "R" (c). The bond occupancy of the M120-Y96/Y122 (black) and M120-W107 (gray) interactions is shown for 3 systems: the unmodified crystal structure (1TNR), the M120-Y122 interacting configuration, and the M120-Y96 interacting configuration (d). M120 interacts stably with W107 in 1TNR. In the M120-Y122 interacting system, M120 interacts somewhat more with Y96/Y122, but still primarily with W107. In the M120-Y96 interacting system, the bond occupancy is reversed - that is, M120 interacts primarily with Y96/Y122 and the W107 interaction is blocked. A snapshot of the Y96 interacting system with Y96 blocking the M120-W107 interaction is shown (e).

Table 1

Interaction energies for DMS or DMSO with benzene, phenol and indole

Results in kcal/mol are computed for fully optimized structures and for conformational ensembles from MD simulations in EtOAc at the MP2/6–311+G(d,p) level and corrected for basis set superposition error. The corresponding structures are reported in Supplementary Figure 2 and uncorrected interaction energies and M06-2X data are shown in Supplementary Table 1.

		Benzene	Phenol	Indole
Full optimization	DMS	−2.4	−4.9	−4.7
	DMSO	−3.3	−10.6	−10.0
Molecular dynamics simulations	DMS	−0.9	−1.0	−1.3
	DMSO Non H-bonded	−1.4	−2.2	−2.7
	DMSO H-bonded		−9.0	−7.5